# Three-Dimensional High-Fidelity Particle Simulations of Gridded Ion Thruster Operation under Ground Testing Conditions

## IEPC-2025-093

Presented at the 39th International Electric Propulsion Conference, Imperial College London, London,
United Kingdom
14-19 September 2025

Gyuha Lim\*, and Deborah A. Levin<sup>†</sup>
University of Illinois Urbana-Champaign, Urbana, Illinois, 61801, USA

This study investigates ground testing effects on gridded ion thruster operation using a combined DSMC and PIC-MCC framework. A computational approach was employed to study gridded ion thruster operation, where the neutral background profile was first characterized through neutral-only DSMC simulations. The results reveal that the chamber pressure is largely uniform but exhibits localized peaks near the thruster and neutralizer exits, underscoring the importance of accounting for the spatially non-uniform neutral backgrounds. Subsequent PIC-MCC simulations were performed under this neutral environment with two different collision models. Even without an externally supplied source of high-energy electrons, inelastic collisions were observed in the near-field due to the strong potential formation at the thruster exit. These inelastic processes reduce the potential, enhance beam neutralization, and reduce beam divergence. Comparisons between cases with and without inelastic collisions demonstrate that neglecting inelastic effects leads to overestimation of both beam divergence and domain size requirements. The findings highlight the critical role of inelastic collisions in accurately modeling gridded ion thruster ground tests.

# Nomenclature

$\bar{c}$	= mean relative speed	200	- ion number density
$\Delta t$	= time step	$n_i$	= ion number density
$\varepsilon_0$	= vacuum permittivity	$\phi$	= electric potential
		p	= pressure
$j_{beam}$	= ion beam current density	q	= elementary charge
$k_B$	= Boltzmann constant	ρ	= charge density
$\lambda_{\mathrm{mfp}}$	= mean free path	'	o v
$\lambda$	= beam divergence	$\sigma$	= collision cross section
$\nu$	= collision frequency	T	= temperature
-	- v	ζ	= relative charge imbalance
$n_e$	= electron number density	v	= particle speed
$n_g$	= neutral gas number density	-	r

<sup>&</sup>lt;sup>†</sup>Professor, Department of Aerospace Engineering, deblevin@illinois.edu.



 $<sup>^*</sup>$ Ph.D. candidate, Department of Aerospace Engineering, gyuhal2@illinois.edu.

## I. Introduction

Despite their growing importance in future space missions, high-power-density gridded ion thrusters face unique challenges during ground testing. Vacuum facility limitations such as high pressure, electrical configuration of the ground testing environment, and sputtered atoms from chamber walls, can result in discrepancies between the ground testing and actual in-space environment. Such discrepancies ultimately affect thruster characterization and may lead to under- or overestimates of key performance metrics such as specific impulse, thrust, and lifetime.

Nishii and Levin investigated these facility effects using three-dimensional Particle-In-Cell (PIC) coupled with Direct Simulation Monte Carlo (DSMC) simulations<sup>6</sup>. By comparing a low-density thruster under both ground-test and in-space conditions, they showed that increased neutral pressure enhances charge-exchange (CEX) and momentum-exchange (MEX) collisions, which in turn form an ion sheath near the chamber walls. Furthermore, Nishii and Levin investigated the effect of neutralizer position and observed the formation of the plasma bridge between the neutralizer and ion beam, showing that considering the neutralizer position is important to fully understand the beam neutralization process.

Recent work by Topham et al.<sup>9</sup> has experimentally demonstrated how undersized facilities and large grounded surfaces can alter the electric field structure, neutralizer coupling, and overall beam divergence in high-power-density ion thrusters. These findings highlight the need for a robust physics-based approach capable of disentangling true thruster behavior from test-chamber artifacts. By focusing on electrical facility effects specifically, such as effects of boundary conditions and sheath formation near chamber walls, we can better understand and correct for potential biases introduced by ground-based testing environments.

While the previous numerical studies<sup>6</sup> employed an idealized thruster geometry with a relatively low plasma density thruster, this work performs three-dimensional particle simulations based directly on the experimental setup of Topham et al.<sup>9</sup>. However, fully resolving the true facility dimensions and grid geometry is computationally prohibitive, therefore, so we adopt a dimensional-scaling strategy to preserve the relevant sheath and collision physics at reduced scale. Specifically, we scale thruster radius, chamber dimension, and plasma screen geometry, while preserving neutral and plasma number densities from the thruster and neutralizer. In a subsequent study, we will carry out full-dimensional simulations to assess the quantitative impact of this scaling and validate the extrapolation of our reduced-scale results to actual dimension conditions.

## II. Computational Methods

This study uses the CUDA-based Hybrid Octree Simulation (CHAOS)<sup>3</sup> to perform three-dimensional particle based simulations. Details of algorithm are given subsections below.

#### A. Direct Simulation Monte Carlo

The DSMC module<sup>1</sup> in this work simulates only the neutral gas flow, representing neutrals as super-particles of weight Fnum. Each DSMC time step  $\Delta t_n$  involves several sequential processes. First, in each computational cell, neutral–neutral collisions are sampled using the No-Time-Counter (NTC) scheme. The collision frequency is computed as

$$\nu_{gg} = n_g \, \sigma_{gg} \, \bar{c}_{gg},\tag{1}$$

where  $n_g$  is the local neutral gas number density,  $\sigma_{gg}$  is the elastic collision cross section between gas particles, and  $\bar{c}_{gg}$  is the mean relative speed between particles.

Once collision pairs are identified, collisions are executed assuming elastic scattering. The post-collision velocities are determined by conserving both momentum and kinetic energy in the center-of-mass frame. Following the collision phase, all neutral super-particles are advanced ballistically over the duration  $\Delta t_n$ . Particles interacting with boundaries are either absorbed or reflected, depending on the specified surface accommodation coefficients.

To ensure physical accuracy, the DSMC time step is selected such that

$$\Delta t_n < 0.1 \, \frac{\lambda_{\rm mfp}}{\bar{c}_{gg}},\tag{2}$$

where  $\lambda_{\rm mfp} = 1/(n_g \, \sigma_{gg}$  is the local mean free path.



#### B. Particle-In-Cell - Monte Carlo Collisions

The PIC-MCC method advances charged super-particles (i.e., ions and electrons) under a self-consistently computed electric field while modeling their collisions with a prescribed background neutral gas. At each time step, typically on the order of picoseconds to nanoseconds, the simulation begins by depositing charge from particles onto the CHAOS<sup>3</sup> Electrical Forest-of-Trees (E-FOT) grid, followed by the solution of Poisson's equation to obtain the electric potential.

$$\nabla^2 \phi = -\frac{\rho}{\varepsilon_0},\tag{3}$$

$$\mathbf{E} = -\nabla \phi,\tag{4}$$

to obtain the electric potential  $\phi$  and electric field **E**. Charged particles are then advanced in phase space using the electric field.

After updating the field and particle pushing, collisions are handled using the null-collision method<sup>5</sup>. For each particle, the probability of undergoing a collision during the time step  $\Delta t$  is given by

$$P = 1 - \exp(-\nu \Delta t), \quad \nu = n_g \sum_k \sigma_k v, \tag{5}$$

where  $n_g$  is the neutral gas number density,  $\{\sigma_k\}$  denotes the cross sections for different collision processes, and v is the ion particle speed.

In this study, for neutral-ion collisions, MEX and CEX collisions are considered. CEX collisions produce slow ions and fast neutrals by transferring an electron from a neutral atom to an ion, whereas momentum-exchange collisions redistribute momentum between colliding particles without altering their charge states. In a recent study by Guita et al.<sup>2</sup>, two-dimensional PIC-MCC simulations were performed for beam neutralization in a gridded-ion thruster. They showed that inelastic collisions between electrons and neutrals play a key role in the neutralization process. This study therefore considers neutral-electron collisions, including elastic, ionization, and four different excitation processes. The cross-section as a function of electron energy shown in Figure 1 are from LXCat<sup>7</sup> database.

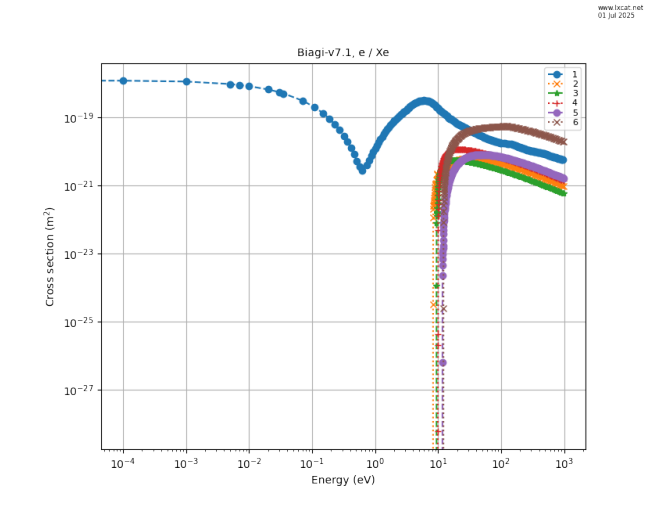


Figure 1: e–Xe collision cross-section data (Biagi-v7.1) from LXCat<sup>7</sup>. 1: elastic, 2–5: excitation, 6: ionization.

## C. Hybrid DSMC-PIC-MCC

Soulas<sup>8</sup> demonstrated that neutral number density distributions during ground testing of gridded ion thrusters are spatially non-uniform. While the PIC–DSMC method can fully resolve this non-uniform neutral background by modeling neutrals as macroparticles, a fully coupled PIC–DSMC simulation is computationally prohibitive and probably not necessary. To supply a spatially varying neutral background for a PIC–MCC simulation, we first perform a cold-flow DSMC simulation to generate the neutral number density and temperature field and then map this field into the PIC–MCC solver. This hybrid approach offers significantly improved computational efficiency, both in memory usage and total runtime, compared to fully coupled PIC–DSMC, while delivering more accurate collision modeling in the vacuum chamber than the assumption of a uniform neutral background. A quantitative comparison of this method will be presented in future work<sup>4</sup>.



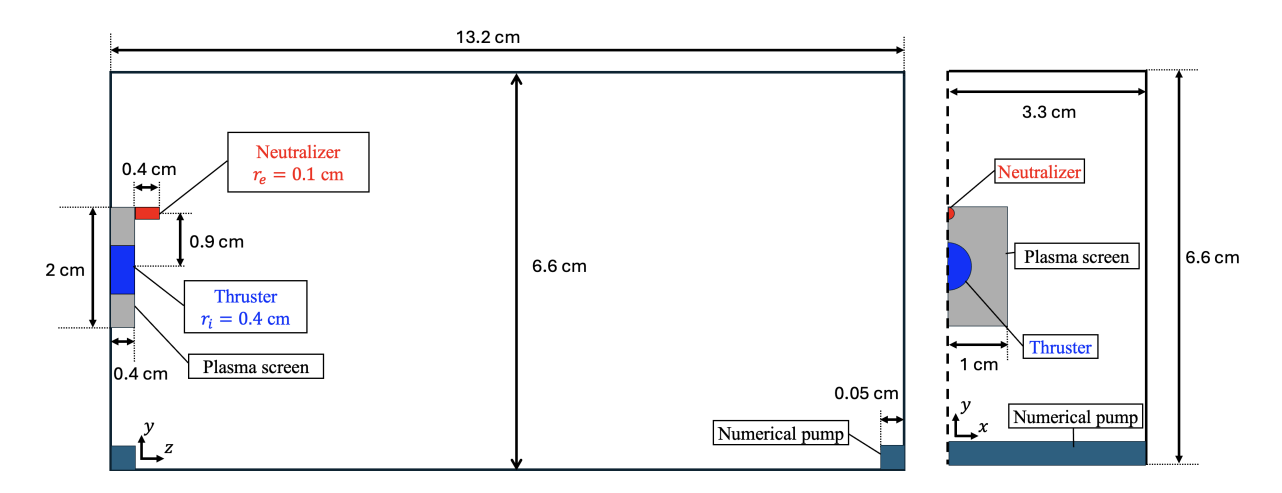


Figure 2: Simulation schematic of the NSTAR-Little Little Brother setup: yz-plane cross-section (left) and xy-plane cross-section (right). Key dimensions are shown in centimeters.  $r_i$  and  $r_e$  refer to the radii of the ion beam thruster and neutralizer, respectively. Figures are not to scale.

# III. Simulation Setup

In this study, we adopt the configuration of the NSTAR-Little Brother device (8 cm diameter) recently described by Topham et al.<sup>9</sup>, itself a reduced-scale version of the original NSTAR thruster. To isolate key physical processes at even smaller scales, we further downscale this configuration by an order of magnitude, creating the NSTAR-Little Little Brother device (0.8 cm diameter). This miniature setup allows us to identify the dominant mechanisms before proceeding to model experiments at the original NSTAR-Little Brother length-scale. Figure 2 presents a schematic of the NSTAR-Little Little Brother geometry. A symmetric boundary condition is imposed on the x-axis, and all other boundaries model the vacuum chamber walls at 300 K, with an accommodation coefficient of unity in the DSMC simulation and charge-absorbing surfaces in the PIC-MCC simulation. The thruster assembly (thruster, neutralizer, and plasma screen) absorbs all charged particles and reflects neutrals. A numerical pump removes any particles that enter its region.

	Thruster		Neutralizer		
Parameter	Xe	${f Xe^+}$	Xe	$\mathbf{e}^{-}$	
Inlet distribution	drift Maxwellian	Gaussian beam (11°)	drift Maxwellian	half Maxwellian	
Number density $(m^{-3})$	$2.6 \times 10^{17}$	$2.3\times10^{15}$	$2.5 \times 10^{18}$	$1.0\times10^{16}$	
Temperature (K)	600	600	1500	1500	
Bulk velocity (m/s)	10	34300	430	-	
Current density (A/m <sup>2</sup> )	-	7.99	_	379.0	
Current (mA)	_	0.40	_	1 10	

Table 1: Inlet conditions at the thruster and neutralizer exits

Table 1 summarizes the species properties at the thruster and neutralizer exits. For the full-scale NSTAR–Little Brother simulation, ion parameters were determined from beam voltage and current provided by Topham et al.<sup>9</sup>, while the neutral mass flow rates were taken from the xenon flow to both the thruster and neutralizer. Neutral temperatures were set to 600 K at the thruster exit and 1500 K at the neutralizer exit, consistent with the 300 °C and 1100 °C values reported by Soulas<sup>8</sup>. At the thruster exit, the neutral bulk velocity was assumed to be a half-Maxwellian corresponding to a temperature of 600 K, whereas the neutral flow inside the neutralizer was assumed to choke, producing a supersonic exit velocity with a bulk speed of 440 m/s corresponding to Mach 1.08. Neutral number densities were computed from the specified temperature, bulk velocity, and mass flow rate. Finally, the electron current was set to  $I_e \approx 3 I_i$ , following Guaita et al.'s sensitivity analysis, which showed minimal impact of  $I_e$  on downstream results<sup>2</sup>.



We then applied dimensional scaling to create the NSTAR–Little Little Brother device, keeping the volume-density quantities (temperature, density, velocity) the same as Little Brother, while absolute currents are reduced by a factor of 100. This miniature setup achieves the same mass utilization (70 %) as the original device, with only the total emitted currents scaled down. Under this configuration, two simulation cases are considered: (A) plume with Xe–Xe<sup>+</sup> momentum-exchange and charge-exchange collisions, and (B) plume with both Xe–Xe<sup>+</sup> and Xe–e collisions.

## IV. Results

#### A. DSMC result for Xe neutral

We first performed a neutral-only DSMC simulation to obtain the background xenon neutral distribution. Figure 3 shows the neutral number density and temperature distributions in the yz-plane at x = 0. In the far-field region, both quantities are nearly uniform due to wall-accommodated neutrals maintained at 300 K. In contrast, elevated density and temperature are observed near the thruster and neutralizer exits, where fresh neutrals are injected into the chamber. This effect is particularly pronounced in front of the neutralizer, where locally heated neutrals raise the temperature above the background level.

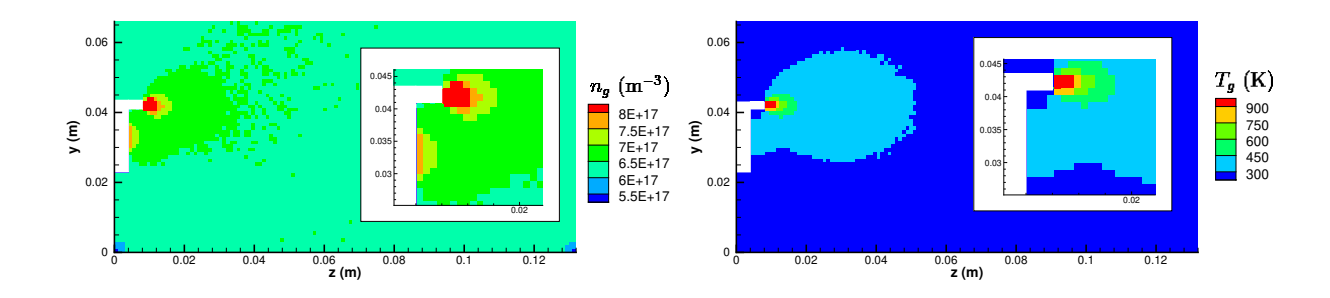


Figure 3: Xenon neutral number density (left) and temperature (right) distribution in the yz-plane at x = 0, where white structure is thruster assembly.

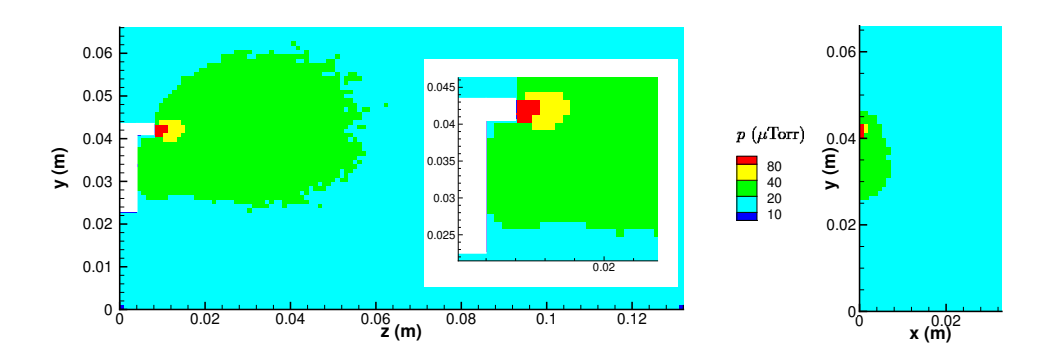


Figure 4: Xenon neutral pressure distribution in the yz-plane at x = 0 m (left), and in the xy-plane at z = 0.009 m (right), where white structure is thruster assembly.

The corresponding pressure distribution from the DSMC results is shown in Figure 4, calculated as  $p = n_g k_B T_g$ . The representative chamber pressure, obtained at the thruster exit plane a short distance from the chamber wall, is about 20  $\mu$ Torr. This value is of the same order of magnitude as the experimentally measured neutral pressure of roughly 40  $\mu$ Torr<sup>9</sup> and remains largely uniform throughout the chamber, except for localized variations near the thruster and neutralizer exits. In particular, the peak pressure near



the neutralizer exit reaches nearly 300  $\mu$ Torr, which enhances Xe–Xe<sup>+</sup> and Xe–e collision frequencies in this region. These findings indicate that a spatially non-uniform neutral background must be considered to more accurately capture collision dynamics near the thruster exit.

#### B. PIC-MCC result for ions and electrons

#### 1. Transient results

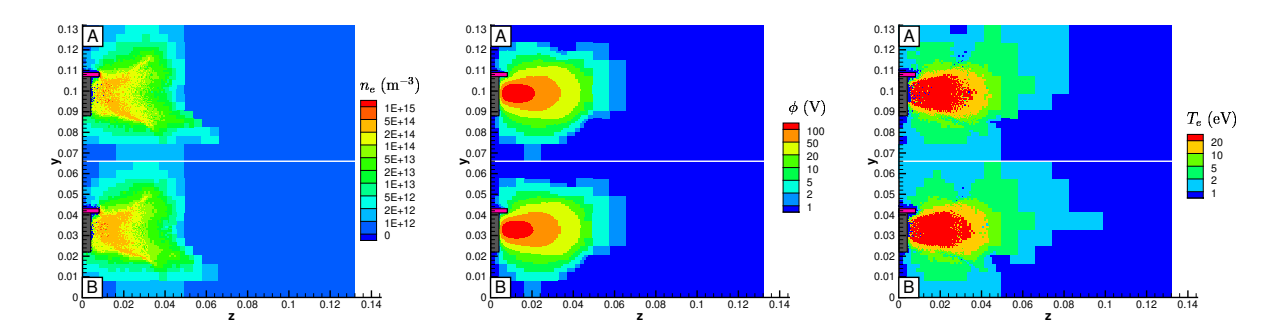


Figure 5: Spatial distributions of electron number density  $(n_e, \text{ left})$ , potential  $(\phi, \text{ center})$  and electron temperature  $(T_e, \text{ right})$  at x = 0 m and t = 1  $\mu$ s. Labels A and B correspond to PIC-MCC simulations with different collision dynamics. The grey structure represents the plasma screen, while the magenta structure represents the neutralizer.

First, we compare the transient results from two simulations at an early time. Figure 5 presents the electron number density, electric potential, and electron temperature at  $t=1~\mu s$ . At this stage, the electron distributions are similar in both cases: electrons emitted from the neutralizer, moving faster than ions, rapidly fill the domain but remain more concentrated near the thruster exit where the ion beam is propagating. A high-potential region forms in front of the thruster exit, pulling and accelerating electrons and generating high-energy electrons in this region. Overall, the potential and electron temperature profiles remain largely similar between cases A and B.

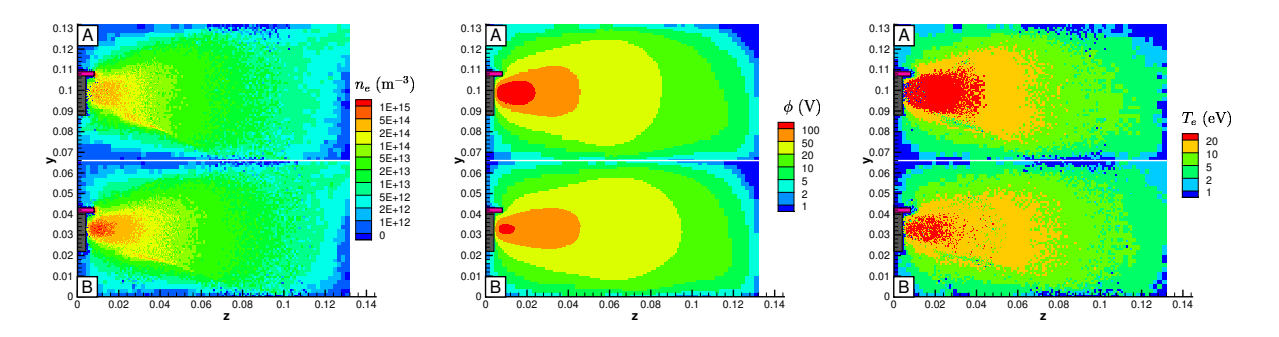


Figure 6: Spatial distributions of electron number density ( $n_e$ , left), potential ( $\phi$ , center) and electron temperature ( $T_e$ , right) at x = 0 m and t = 5  $\mu$ s. Labels A and B correspond to PIC-MCC simulations with different collision dynamics. The grey structure represents the plasma screen, while the magenta structure represents the neutralizer.

Next, Figure 6 shows the results at  $t = 5 \mu s$ . By this time, the beam ions have reached the end wall, and the two cases exhibit clear differences in electron density. Case A shows a reduced electron population, while case B contains more electrons due to ionization. Electron energy loss processes also lead to electron trapping near the thruster exit, resulting in localized electron clouds. The electric potential and electron temperature reflect these differences: case A exhibits a higher potential near the thruster exit and elevated



electron temperature, whereas in case B both the peak potential and electron temperature decrease because of energy losses from excitation and ionization.

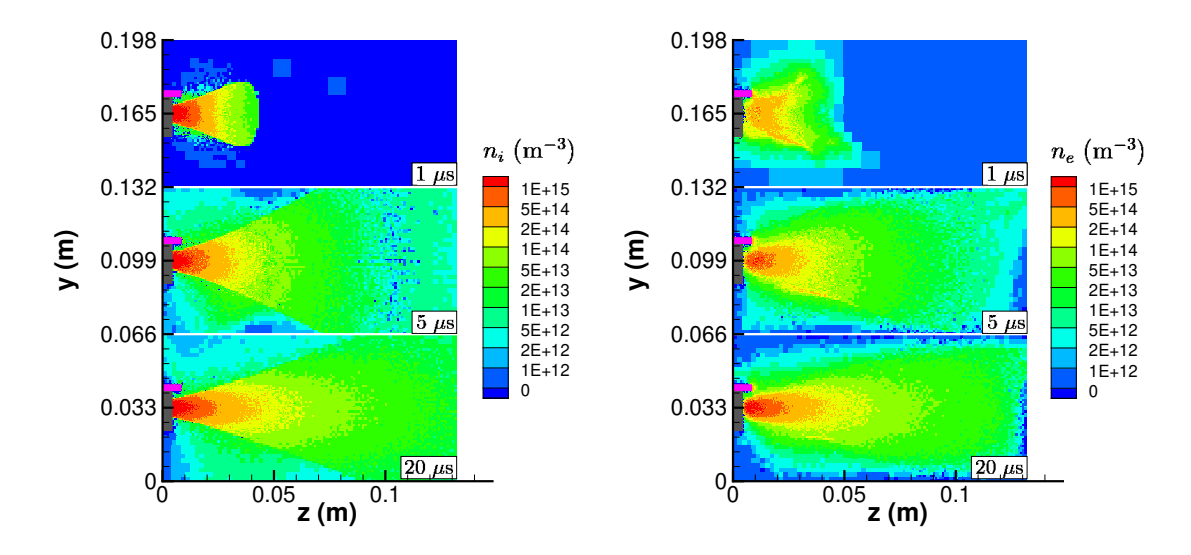


Figure 7: Distributions of  $n_i$  (left), and  $n_e$  (right) at x=0 m and t=1  $\mu s$  (top), t=5  $\mu s$  (middle), and t=20  $\mu s$  (bottom). The grey structure represents the plasma screen, while the magenta structure represents the neutralizer. Note that the blue dots appearing in the ion number density contour at t=5  $\mu s$  are transient effects caused by adaptive mesh refinement at that moment.

Primary electrons, defined as the electrons emitted from the neutralizer, have a mean energy of approximately 2 eV, insufficient to induce inelastic collisions, as this is below the excitation and ionization thresholds. However, the strong potential peak near the thruster exit accelerates some electrons to energies exceeding 20 eV (see Figure 5), where the inelastic collision cross sections, particularly for ionization, surpass those for elastic collisions (see Figure 1). Consequently, electrons from the neutralizer gain sufficient energy to undergo inelastic collisions, producing additional ions and electrons via ionization while also losing energy through excitation collisions. Therefore, although both cases exhibit high potential and electron temperature at  $t=1~\mu s$ , case B at  $t=5~\mu s$  shows reduced peak potential and electron temperature due to these enhanced inelastic processes.

While case A approaches steady state by  $t=10~\mu s$ , case B requires a longer timescale (around  $t=25~\mu s$ ) to reach steady state due to the additional slow ion formation associated with the ionization process. Figure 7 shows the temporal evolution of the ion and electron number densities for case B at  $t=1~\mu s$ ,  $t=5~\mu s$ , and  $t=20~\mu s$ . The ion number density contours show a steadily increasing ion population inside the beam region, resulting from additional ion production through ionization. These newly generated slow ions remain longer in the computational domain, as their lower velocities delay transport to the boundaries. In the electron number density contours, dense electron clouds emerge near the thruster exit, signifying improved beam neutralization. This occurs because electrons lose energy through inelastic collisions and become more easily confined near the exit. In contrast, such dense electron structures are absent in case A, where electron energy-loss mechanisms are not included.

Figure 8 presents the corresponding electric potential and electron temperature distributions. The potential contours show a gradual decay of the peak near the thruster exit, consistent with enhanced charge neutralization by the electron clouds. As a consequence, the initially elevated electron temperature progressively decreases with time. In the early stage of thruster operation, a strong potential peak accelerates and heats electrons. These high-energy electrons undergo frequent inelastic collisions, losing energy primarily through excitation and ionization while simultaneously producing additional ions. This process reduces the potential near the exit, leading to fewer electrons being accelerated to high energies. Ultimately, the rate of inelastic collisions, while peaking in the initial stage, gradually diminishes as the system approaches steady state.



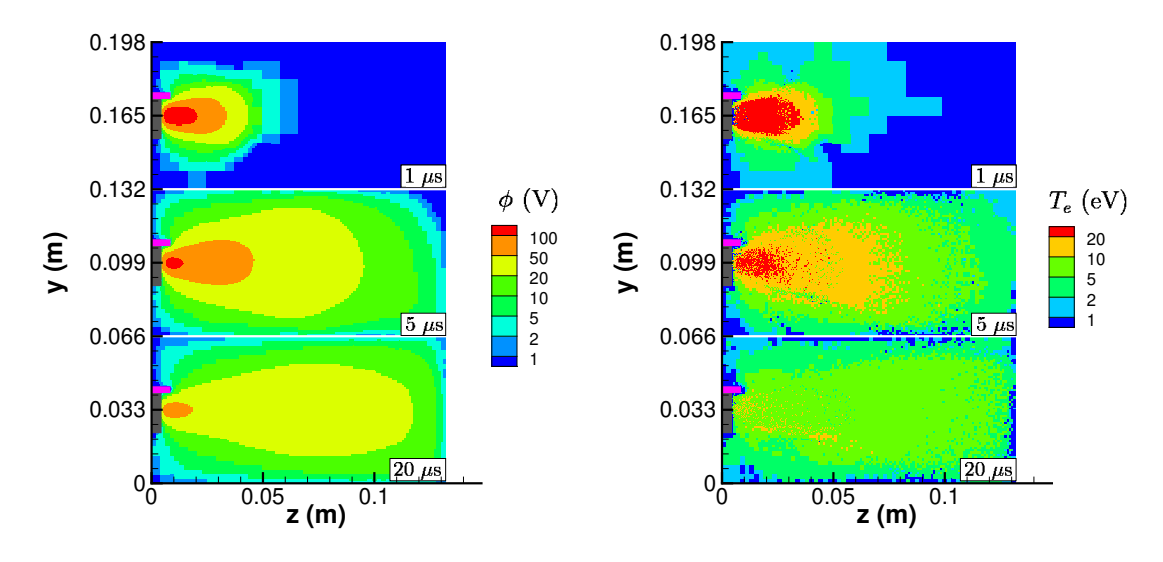


Figure 8: Distributions of  $\phi$  (left), and  $T_e$  (right) at x = 0 m and t = 1  $\mu$ s (top), t = 5  $\mu$ s (middle), and t = 20  $\mu$ s (bottom). The grey structure represents the plasma screen, while the magenta structure represents the neutralizer.

#### 2. Steady-state result

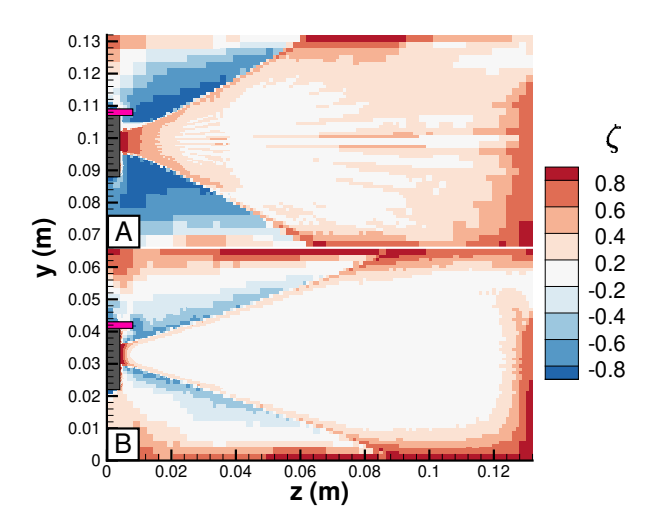


Figure 9: Relative charge imbalance  $(\zeta)$  contour at x = 0 for case A(top) and case B(bottom).

After reaching steady state, both simulations were sampled to reduce statistical noise. We quantify quasi-neutrality using the relative charge imbalance

$$\zeta \equiv \frac{n_i - n_e}{n_i + n_e}. (6)$$

Here,  $\zeta \approx 0$  (white) indicates quasi-neutrality;  $\zeta > 0$  (red) is ion-rich; and  $\zeta < 0$  (blue) is electron-rich. Within the main beam,  $\zeta$  remains near zero for case B (see Figure 9), indicating effective neutralization. However, for case A, the lack of an electron energy-loss mechanism prevents the ion beam from efficiently trapping electrons. Instead, electrons are absorbed by the chamber walls, resulting in electron depletion as described by Nishii and Levin<sup>6</sup>. Consequently, more ion-rich regions form within the beam. In addition, the more reddish regions near the thruster exit in case A further highlight its poorer neutralization compared with case B.

In agreement with Guaita et al.<sup>2</sup>, inelastic collisions are a key process strongly influencing beam neutralization. In addition, our results show ion-rich layers adjacent to the chamber walls, consistent with sheath formation, and electron-rich regions in the near-field plume wings, reflecting electron attraction toward the positively charged beam.

We extracted line profiles averaged over x = 0 to 0.003 m, including the plume axis at y = 0.033 m and cross-lines at z = 0.02 m and z = 0.10 m, to enable direct comparison between the two cases. Figure 10 presents the ion and electron number densities along the plume axis. Although the peak ion number density near the thruster exit is nearly identical, case A exhibits a faster decay compared to case B. In both cases,



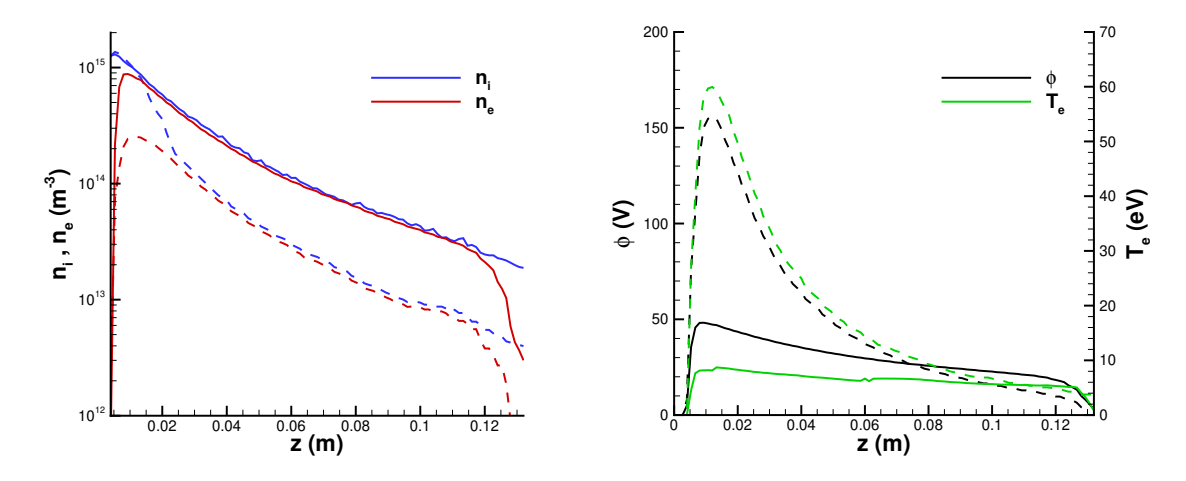


Figure 10: Profiles along the plume axis (y = 0.033 m), extracted from slice-averaged data over x = 0 to 0.003 m. Left: Ion (blue) and electron (red) number densities. Right: Plasma potential  $\phi$  (black) and electron temperature  $T_e$  (green). Solid lines correspond to case B, and dashed lines correspond to case A.

sheath formation is observed near the thruster exit and the end wall, indicated by the sudden drop in electron density. The electron number density shows a pronounced difference, as inelastic collisions strongly affect electron behavior. Specifically, the peak electron density in case B is almost four times higher than in case A, providing clear evidence of electron clouds and improved neutralization. This enhanced neutralization in case B also reduces the peak plasma potential in front of the thruster exit. Consequently, case B maintains lower potential and electron temperature values than case A near the exit region.

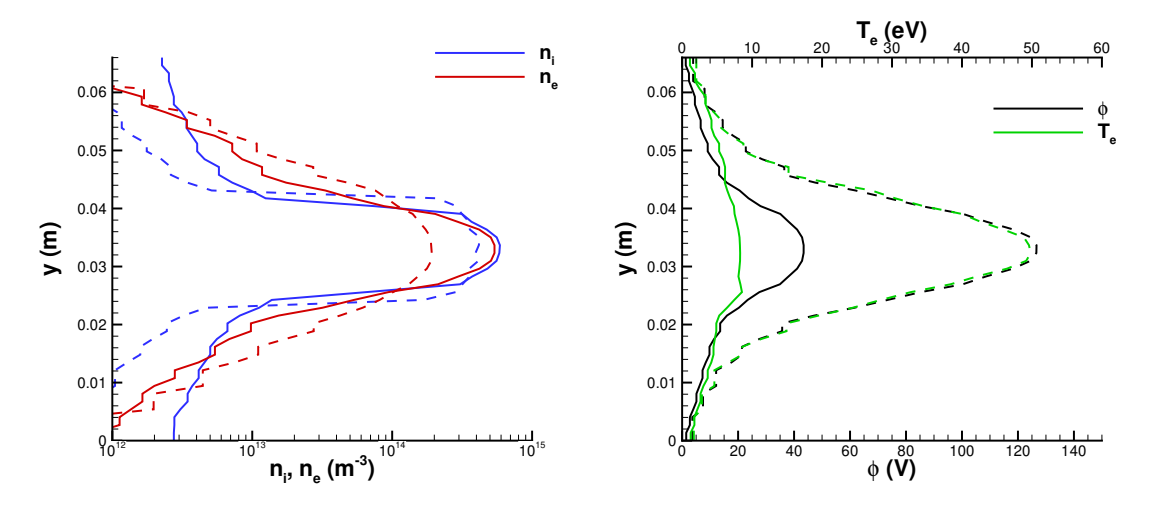


Figure 11: Profiles along the cross-line (z=0.02 m), extracted from slice-averaged data over x=0 to 0.003 m. Left: Ion (blue) and electron (red) number densities. Right: Plasma potential  $\phi$  (black) and electron temperature  $T_e$  (green). Solid lines correspond to case B, and dashed lines correspond to case A.

Figure 11 shows the crossline profiles at z=0.02 m, corresponding to the near-field region close to the thruster exit. In case A, the insufficient electron population near the axis leads to a clear charge imbalance, resulting in an elevated plasma potential and higher electron temperature as the system attempts to attract additional electrons. In contrast, case B benefits from inelastic electron collisions that generate new electrons through ionization and from electron energy loss that traps electrons near this region, thereby improving charge balance. Consequently, case B exhibits higher peak ion densities and a more rounded



front, preserving the Gaussian beam characteristics at the inlet, whereas case A produces a flattened ion distribution. The electron density in case B follows the ion beam but, due to their higher mobility, electrons extend farther outward, creating a transition from ion-dominated to electron-dominated regions near the beam edge. Consistently, case B displays a broader electron distribution and higher electron temperature than case A. Near the sidewalls, however, the ion population becomes dominant again due to sheath formation at the boundaries. We expected to observe quasi-neutral regions outside the beam before the onset of the plasma sheath. However, at this location no such region is present, which we attribute to the limited domain size. The sheath effects appear to extend into the solution, suggesting that a larger domain will be required in future simulations.

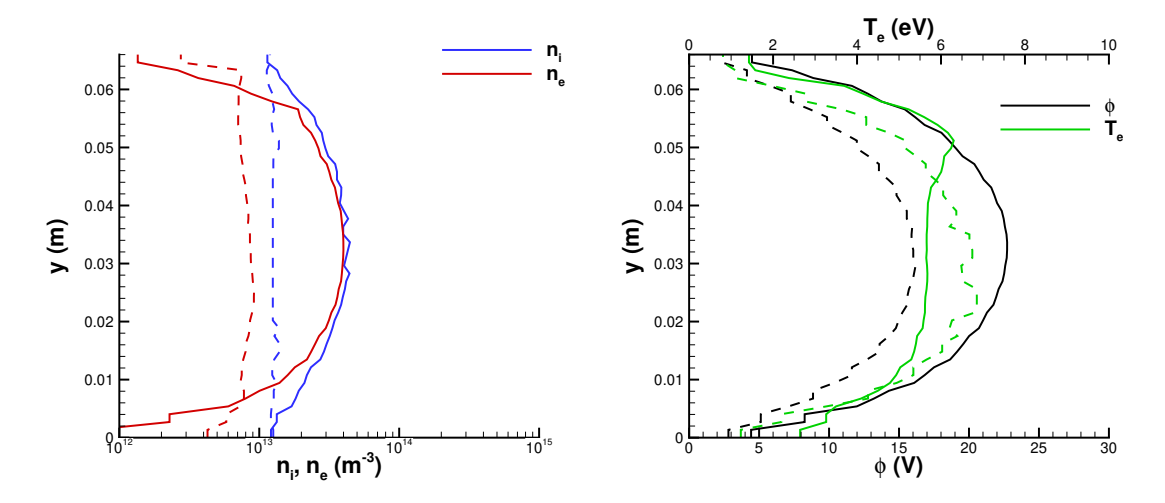


Figure 12: Profiles along the cross-line (z=0.10 m), extracted from slice-averaged data over x=0 to 0.003 m. Left: Ion (blue) and electron (red) number densities. Right: Plasma potential  $\phi$  (black) and electron temperature  $T_e$  (green). Solid lines correspond to case B, and dashed lines correspond to case A.

Figure 12 shows the crossline profiles at z=0.10 m, corresponding to the far-field region where the beam reaches the sidewalls in both cases. At this location, both ion and electron number densities, as well as the plasma potential and electron temperature, have decayed relative to the near field. Case B still maintains higher overall densities, and distinct sheath formation is evident from the sharp drop in electron density near the sidewalls. In contrast, the plasma potential and electron temperature profiles of cases A and B are similar in magnitude at this distance.

To study beam characteristics, we computed the beam current and beam divergence at different z locations from the sampled solution. The beam current on a plane located at  $z=z_0$  is obtained by integrating the axial current density  $j_{beam}=q\,n_i\,u_z$ ,

$$I_B(z_0) = \int_{A(z=z_0)} j_{beam}(x, y, z_0) dA,$$
 (7)

The beam divergence angle is

$$\lambda(z_0) = \cos^{-1} \left( \frac{\int_{A(z=z_0)} j_{beam} \frac{u_z}{\sqrt{u_x^2 + u_y^2 + u_z^2}} dA}{I_B(z_0)} \right), (8)$$

Here,  $A(z_0) = \{(x, y) : z = z_0\}$  is the sampling plane, and the ion velocities  $(u_x, u_y, u_z)$  are evaluated from the sampled data on this plane and vary with (x, y).

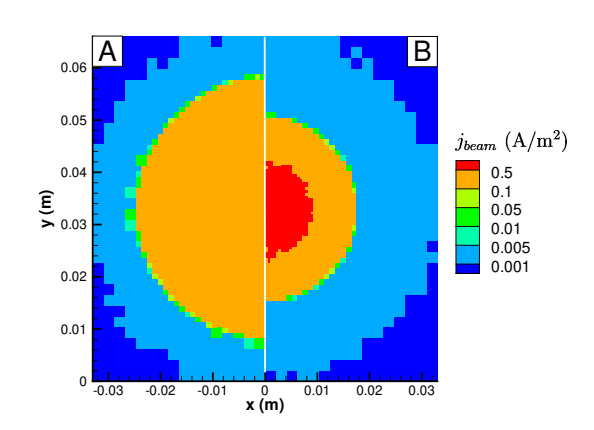


Figure 13: Ion beam current density  $(j_{beam})$  of case A (left) and case B (right) at z = 0.05 m.



Figure 13 shows the ion beam current density contour at z=0.05 m. We can see that case B exhibits a higher current density at the center, indicating a more collimated beam. Figure 14 shows the beam current and beam divergence as functions of z, computed at discrete planes from z=0.01 to 0.13 in increments of 0.01. Initially, the beam current remains close to the imposed value of 0.4 mA for both cases, with only a slight decrease as the beam propagates. For case A, however, a sharp drop occurs after z=0.06 m, as the beam begins to strike the sidewalls due to its larger divergence (right panel of Figure 14), leading to ion loss and particle deletion. In contrast, case B maintains a smaller divergence angle, keeping the beam more collimated and preserving the current further downstream, up to about z=0.09 m. These results indicate that ionization contributes to improved beam collimation by enhancing the neutralization process.

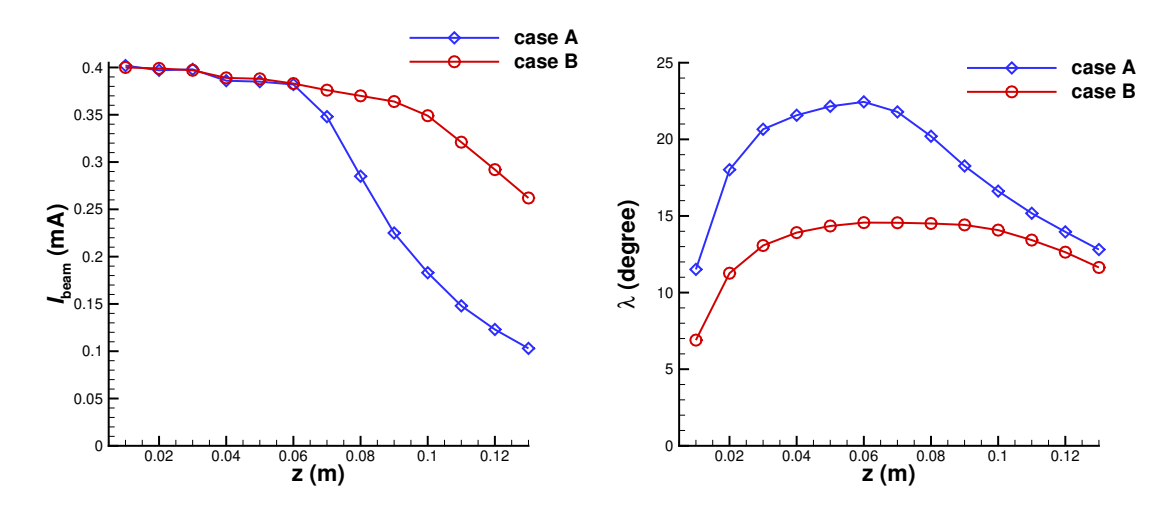


Figure 14: Beam current (left) and current-weighted divergence angle (right) versus axial position z, evaluated on planes from z = 0.01 to 0.13 m in 0.01 m steps. For beam divergence from z = 0.07 m (case A) and z = 0.09 m (case B), values are shown for completeness but may be affected by wall loses.

## V. Conclusion

In this study, we employed a scaled setup of a gridded ion thruster ground test to investigate its operation. First, the neutral background profile was obtained using neutral-only DSMC simulations. The results showed that the background pressure is generally consistent throughout the chamber but exhibits localized peaks near the thruster and, in particular, the neutralizer exit, highlighting the importance of accounting for a spatially non-uniform neutral background. Next, we performed PIC-MCC simulations under this neutral background with two different collision models. Even without introducing sufficiently high energy electrons to directly drive inelastic collisions, we observed that such collisions occur in the early stages due to the strong potential near the thruster exit. These inelastic processes gradually reduce the high potential value while also enhancing beam neutralization. Consequently, neglecting inelastic collisions will lead to overestimation of the beam divergence and, in turn, overprediction of the required domain size. In future work, we plan to extend this study by simulating a more realistic experimental configuration that incorporates inelastic collisions, enabling a deeper understanding of how ground test facilities influence gridded ion thruster operation.

## Acknowledgments

This work was partially supported by NASA through the Joint Advanced Propulsion Institute, a NASA Space Technology Research Institute, grant number 80NSSC21K1118. This work used Delta at the National Center for Supercomputing Applications (NCSA) through allocation PHY220158.



#### References

<sup>1</sup>Bird, G. A., *Molecular Gas Dynamics and the Direct Simulation of Gas Flows*, Clarendon Press, Oxford, 1994.

<sup>2</sup>Guaita, M., Marín-Cebrián, A., Merino, M., Ahedo, E., Cipriani, F., and Dannenmayer, K., "Electron Populations and Neutralization Process in the Plume of a Gridded Ion Thruster," *Plasma Sources Science and Technology*, Vol. 34, Apr. 2025.

<sup>3</sup>Jambunathan, R., and Levin, D. A., "CHAOS: An Octree-Based PIC-DSMC Code for Modeling of Electron Kinetic Properties in a Plasma Plume Using MPI-CUDA Parallelization," *Journal of Computational Physics*, Vol. 373, Nov. 2018, pp. 571–604.

<sup>4</sup>Lim, G., and Levin, D. A., "Hybrid DSMC and PIC-MCC Method with Spatially Varying Pressure for Electric Propulsion Ground Testing," *Proceedings of the AIAA SciTech Forum (SciTech2026)*, AIAA, Reston, VA, 2026 (to be presented).

<sup>5</sup>Nanbu, K., "Theory of Cumulative Small-Angle Collisions in Plasmas," *Physical Review E*, Vol. 55, No. 4, 1997, pp. 4642–4652.

<sup>6</sup>Nishii, K., and Levin, D. A., "Kinetic Simulation of Ion Thruster Plume Neutralization in a Vacuum Chamber," *Plasma Sources Science and Technology*, Vol. 32, No. 11, 2023, Paper 115009.

<sup>7</sup>Pitchford, L. C., Alves, L. L., Bartschat, K., Biagi, S. F., Bordage, M. C., Bray, I., Brion, C. E., Brunger, M. J., Campbell, L., Chachereau, A., Chaudhury, B., Christophorou, L. G., Carbone, E., Dyatko, N. A., Franck, C. M., Fursa, D. V., Gangwar, R. K., Guerra, V., Haefliger, P., Hoesl, A., Itikawa, Y., Kochetov, I. V., McEachran, R. P., Morgan, W. L., Napartovich, A. P., Puech, V., Rabie, M., Sharma, L., Srivastava, R., Stauffer, A. D., Tennyson, J., de Urquijo, J., van Dijk, J., Viehland, L. A., Zammit, M. C., Zatsarinny, O., and Pancheshnyi, S., "LXCat: An Open-Access, Web-Based Platform for Data Needed for Modeling Low Temperature Plasmas," *Plasma Processes and Polymers*, Vol. 14, No. 1–2, 2017, Paper 1600098.

<sup>8</sup>Soulas, G. C., "Modeling Neutral Densities Downstream of a Gridded Ion Thruster," *Journal of Propulsion and Power*, Vol. 27, No. 3, May–June 2011, pp. 538–548.

<sup>9</sup>Topham, T. J., Judge, J., Baker, J., and Foster, J. E., "Facility Effects on Gridded Ion Engine Operation," *Proceedings of the 38th International Electric Propulsion Conference*, IEPC-2024-771, Electric Rocket Propulsion Society, 2024.

